

Magneto-inertial range dominated by magnetic helicity in space plasmas

A. Bershadskii

ICAR, P.O. Box 31155, Jerusalem 91000, Israel

Magneto-inertial range dominated by magnetic helicity has been studied using results of the numerical simulations, laboratory measurements, solar, solar wind, and Earth's magnetosphere observations (spacecraft measurements). The spectral data have been compared with the theoretical results obtained on the basis of the distributed chaos notion in the frames of the Kolmogorov-Iroshnikov phenomenology. The transition from magnetohydrodynamics to kinetics in the solar wind and at the special events (reconnection and Kelvin-Helmholtz instability) in Earth's magnetosphere has been discussed in this context.

I. INTRODUCTION

There are three quadratic invariants of the ideal magnetohydrodynamics. Total energy, magnetic and cross helicity. In this paper, we will be concentrated on the former two. The magnetic helicity can be defined as

$$h_m = \langle \mathbf{a} \mathbf{b} \rangle \quad (1)$$

where $\mathbf{b} = [\nabla \times \mathbf{a}]$ is the fluctuating magnetic field, and $\langle \dots \rangle$ denotes a spatial average (both \mathbf{a} and \mathbf{b} have zero means, and $\nabla \cdot \mathbf{a} = 0$). Under a uniform mean magnetic field \mathbf{B}_0 the magnetic helicity is not an invariant. In the paper Ref. [1] a modified magnetic helicity was introduced in the form

$$\hat{h}_m = h_m + 2\mathbf{B}_0 \cdot \langle \mathbf{A} \rangle \quad (2)$$

where $\mathbf{B} = \mathbf{B}_0 + \mathbf{b}$, $\mathbf{A} = \mathbf{A}_0 + \mathbf{a}$, and $\mathbf{b} = [\nabla \times \mathbf{a}]$. It is shown in the paper [1] that at certain (rather weak) restrictions on the boundary conditions

$$\frac{d\hat{h}_m}{dt} = 0 \quad (3)$$

in the ideal magnetohydrodynamics.

In hydrodynamic turbulence existence of an inertial range of scales with statistical characteristics depending only on the kinetic energy dissipation rate ε (but not on the molecular viscosity) is expected for the high Reynolds numbers [2]. Analogously, in magnetohydrodynamics (MHD) a magneto-inertial range of scales dominated by magnetic helicity can be introduced. In this case, we have two governing parameters the total energy (kinetic plus magnetic) dissipation rate ε and the magnetic helicity dissipation rate ε_h . A similar situation (two governing parameters - kinetic dissipation rate and its analogy for the passive scalar) was considered for the so-called inertial-convective range of passive scalar turbulent mixing (the Corrsin-Obukhov approach [2]), and in Section III we will use analogous approach to the magneto-inertial range of scales, but in the frames of the distributed chaos notion.

In Section IV the theoretical results will be compared with the results of observations in the solar wind (the spacecraft measurements produced at different distances

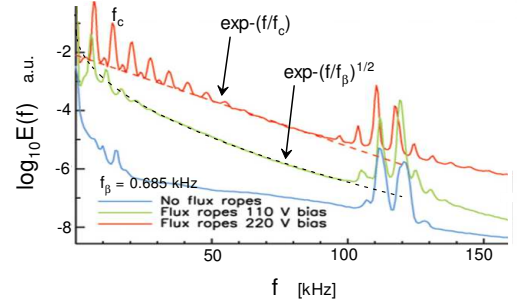


FIG. 1: Traces of average magnetic field power spectra measured in a laboratory experiment (the Large Plasma Device at UCLA) studying chaos in motions of magnetic flux ropes immersed in a magnetized helium plasma.

from the Sun: from 0.16 AU to 4.5 AU). In Section V transition from magnetohydrodynamics to kinetics will be studied within the deterministic and distributed chaos approach (in the latter case on the magneto-inertial range of scales). Comparison with results of numerical simulations, laboratory experiments, and observations in the solar wind and at special events (reconnection jet and Kelvin-Helmholtz vortices) in the Earth's magnetosphere will be made in Section V.

II. DISTRIBUTED CHAOS

Deterministic chaos (at the onset of turbulence) is often characterized by the exponential power spectra (both temporal and spatial)[3]-[6]

$$E(f) \propto \exp(-f/f_c) \quad (4)$$

and/or

$$E(k) \propto \exp(-k/k_c) \quad (5)$$

where f is frequency, k is wavenumber.

Figure 1, for instance, shows (in the linear-log scales) the traces of average magnetic field power spectra measured in a laboratory experiment (the Large Plasma

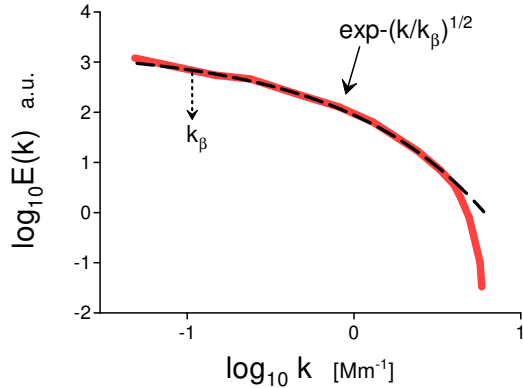


FIG. 2: The spot and noise corrected magnetic power spectrum for the solar active region NOAA 8375.

Device at UCLA) studying chaos in motions of magnetic flux ropes (magnetic structures with helical currents and magnetic fields) immersed in a magnetized helium plasma [7]. The magnetic flux ropes rotate about a central axis in a cylindrical vessel, writhe about each other, twist about themselves, and are kink unstable. Collisions between the magnetic ropes result in magnetic field lines reconnection.

According to Taylor's "frozen in" hypothesis the experimental spectrum shown in Fig. 1 should be interpreted as a wavenumber spectrum with $k \simeq 2\pi f/V_0$, where V_0 is the mean speed of the spatial magnetic structures passing the probe (cf., for instance, Refs. [5],[8] and references therein). The dashed straight line is drawn through the upper curve in Fig. 1 to indicate the exponential spectrum Eq. (5) corresponding to the spatial *deterministic* chaos.

Changing the parameter driving the magnetic flux ropes in the experiment one can make the characteristic scale k_c in Eq. (5) fluctuate, then in order to compute the magnetic power spectra one needs an ensemble averaging

$$E(k) \propto \int_0^\infty P(k_c) \exp(-(k/k_c)dk_c) \quad (6)$$

where a probability distribution $P(k_c)$ characterizes the fluctuations of the characteristic scale k_c .

To find the probability distribution $P(k_c)$ in the plasma dominated by the magnetic helicity one can use a scaling relationship between characteristic values of the magnetic field B_c and k_c

$$B_c \propto |h_m|^{1/2} k_c^{1/2} \quad (7)$$

obtained with the dimensional considerations. If the B_c has a normal distribution (Gaussian with zero mean [2]), then k_c has the chi-squared (χ^2) distribution

$$P(k_c) \propto k_c^{-1/2} \exp(-(k_c/4k_\beta) \quad (8)$$

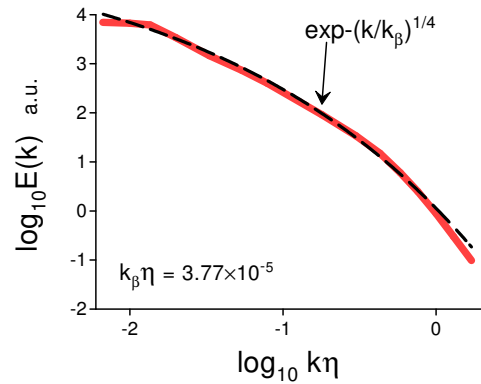


FIG. 3: Magnetic energy spectrum for the DNS with considerable mean magnetic helicity.

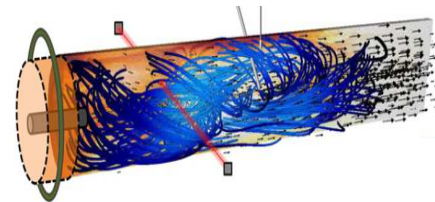


FIG. 4: A sketch of the MHD (plasma gun) wind tunnel.

where k_β is a new characteristic constant.

Substituting Eq. (8) into Eq. (6) one obtains

$$E(k) \propto \exp(-(k/k_\beta)^{1/2} \quad (9)$$

This is the magnetic energy spectrum in the non-dissipative range of scales dominated by the magnetic helicity for a *distributed* chaos.

The dashed curve is drawn through the middle curve in Fig. 1 to indicate the stretched exponential spectrum Eq. (9) corresponding to the spatially distributed chaos dominated by magnetic helicity. In this case, the considered (experimental) spatial domain is not enclosed completely by a magnetic flux surface, then \mathbf{a} is not gauge invariant. In this case a gauge-invariant relative magnetic helicity with an appropriate reference magnetic field (the axial background magnetic field - constant in time and space outside the experimental vessel,) can be used instead [9],[10],[11].

It is well known that multiple flux ropes extend from the solar surface into the solar photosphere and corona. Coronal Mass Ejections can be triggered by the multiple flux ropes collisions [12].

In Ref. [13] results of the space-based (SOHO/MDI) spectral measurements of the longitudinal magnetic fields in the solar active region NOAA 8375 (made on 4 November 1998) were reported. At the time of the measurements, the active region was located at the center of the solar disk. To avoid the strong contribution of the sunspot to the power spectrum the authors of the Ref. [13] blocked out the sunspot. Figure 2 shows the spot and noise corrected magnetic power spectrum (the spectral data were taken from Fig. 6b of the Ref. [13]). The dashed curve is drawn to indicate the stretched exponential spectrum Eq. (9) corresponding to the spatially distributed chaos dominated by magnetic helicity (cf Ref. [14]).

Magnetic ropes are routinely ejected from the Sun. These magnetic flux ropes can transport a large amount of magnetic helicity into the solar wind.

III. MAGNETO-INERTIAL RANGE OF SCALES

Conditions in the solar wind are significantly different from those in the solar atmosphere. The main difference is the high speed of the plasma moving away from the Sun. Therefore, a different phenomenology - magneto-inertial range (see Introduction) should be used for the solar wind. In this case, the estimate Eq. (7) should be replaced by

$$B_c \propto \varepsilon_h^{1/2} \varepsilon^{1/6} k^{1/6} \quad (10)$$

(cf the Corrsin-Obukhov phenomenology for the inertial-convective range [2]).

If a significant mean magnetic field is present, then the energy dissipation rate ε in Eq. (7) should be replaced by a more appropriate parameter ($\varepsilon \tilde{B}_0$) (here $\tilde{B}_0 = B_0/\sqrt{\mu_0 \rho}$ is the normalized mean magnetic field, having the same dimension as velocity) [15]. The dimensional considerations, in this case, results in

$$B_c \propto \varepsilon_h^{1/2} (\varepsilon \tilde{B}_0)^{1/8} k^{1/8} \quad (11)$$

with the modified magnetic helicity (see the Eq. (2)) dissipation rate $\varepsilon_{\tilde{h}}$.

The estimates Eq. (10-11) can be generalized as

$$B_c \propto k^\alpha \quad (12)$$

Let us, following Eq. (9), seek the spectrum for the distributed chaos as a stretched exponential one

$$E(k) \propto \int_0^\infty P(k_c) \exp(-(k/k_c)^\beta) dk_c \propto \exp(-(k/k_\beta)^\beta) \quad (13)$$

For large k_c the probability distribution $P(k_c)$ can be estimated from the Eq. (13) as [16]

$$P(k_c) \propto k_c^{-1+\beta/[2(1-\beta)]} \exp(-\gamma k_c^{\beta/(1-\beta)}) \quad (14)$$

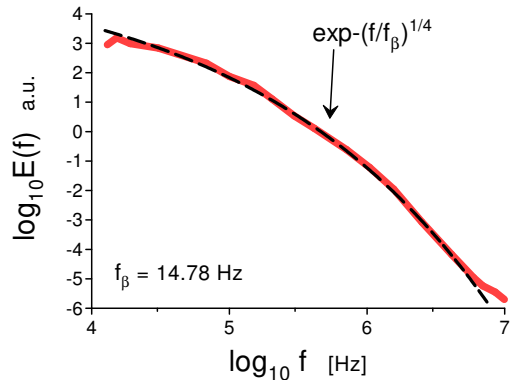


FIG. 5: Ensemble averaged total magnetic energy spectrum measured in the MHD (plasma gun) wind tunnel experiment.

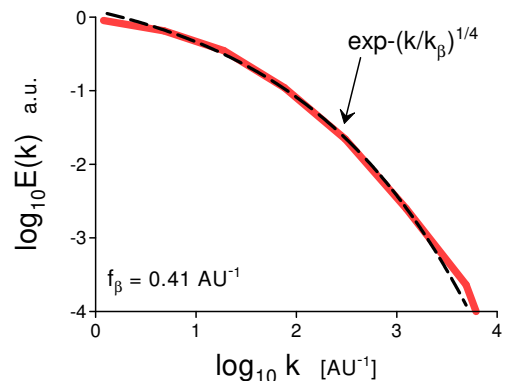


FIG. 6: Total magnetic energy spectrum for the fast solar wind at $2.8 < R < 4.5$ AU (Ulysses, 1993-1996yy).

Then, using some algebra, the relationship between the exponents β and α can be readily obtained for the normally distributed B_c

$$\beta = \frac{2\alpha}{1+2\alpha} \quad (15)$$

Hence, for $\alpha = 1/6$ (see Eq. (10))

$$E(k) = \exp(-(k/k_\beta)^{1/4}) \quad (16),$$

and for $\alpha = 1/8$ (see Eq. (11))

$$E(k) = \exp(-(k/k_\beta)^{1/5}) \quad (17)$$

These are spatial magnetic power spectra in the magneto-inertial range of scales dominated by magnetic helicity.

The magnetohydrodynamic equations for incompressible homogeneous plasma in the Alfvénic units are

$$\frac{\partial \mathbf{u}}{\partial t} = -\mathbf{u} \cdot \nabla \mathbf{u} - \frac{1}{\rho} \nabla \mathcal{P} - [\mathbf{b} \times (\nabla \times \mathbf{b})] + \nu \nabla^2 \mathbf{u} + \mathbf{f} \quad (18),$$

$$\frac{\partial \mathbf{b}}{\partial t} = \nabla \times (\mathbf{u} \times \mathbf{b}) + \eta \nabla^2 \mathbf{b} \quad (19),$$

$$\nabla \cdot \mathbf{u} = 0, \quad \nabla \cdot \mathbf{b} = 0, \quad (20, 21)$$

where \mathbf{u} and $\mathbf{b} = \mathbf{B}/\sqrt{\mu_0 \rho}$ are velocity and normalized magnetic field, and \mathbf{f} is a forcing function.

In the paper Ref. [17] a direct numerical simulation using the Eqs. (18-21) without mean magnetic field was performed in a 3D spatial box (periodic boundary conditions). The initial fields were randomly generated with kinetic and magnetic energies equal to 0.5 (in the terms of the Ref. [17]). The initial mean cross helicity was taken almost zero, while the initial mean (normalized) magnetic helicity was rather considerable - 0.515 (at the statistically stationary state the normalized mean magnetic helicity was 0.655). The large-scale random forcing \mathbf{f} was concentrated in the wavenumber range $1 < k < 2.5$. The magnetic Prandtl number $Pr_m = \nu/\eta = 1$, the Taylor-Reynolds number $R_\lambda = 150$ and the magnetic Reynolds number $R_\lambda^{(m)} = 306$.

Figure 3 shows the magnetic energy spectrum computed for the statistically stationary state using a wavelet method (η is a dissipation scale). The spectral data were taken from Fig. 1 of the Ref. [17]. The dashed curve indicates correspondence to the stretched exponential spectrum Eq. (16) (for freely *decaying* MHD turbulence with considerable mean magnetic helicity see Fig. 17).

Figure 4 (adapted from the Ref. [8]) shows a sketch of the MHD (plasma gun) wind tunnel. This experiment can imitate situations similar to those typical for solar wind. The blue lines in the figure show twisting of the magnetic field lines due to magnetic helicity conservation.

Figure 5 shows the ensemble-averaged total magnetic energy spectrum measured in the experiment. The spectral data were taken from Fig. 15a of the Ref. [8]. Taylor's "frozen in" hypothesis can be used to transform the measured frequency spectrum to the more adequate in this case wavenumber spectrum. The dashed curve indicates correspondence to the stretched exponential spectrum Eq. (16).

IV. SOLAR WIND

Solar wind is characterized by a wide variety of physical conditions. Therefore it is a unique natural MHD laboratory.

Figure 6, for instance, shows the total magnetic energy spectrum calculated using measurements made by Ulysses mission for the 1993-1996y period at the high heliolatitudes and in the fast solar wind. The spectral data were taken from Fig. 3 of the Ref. [18]

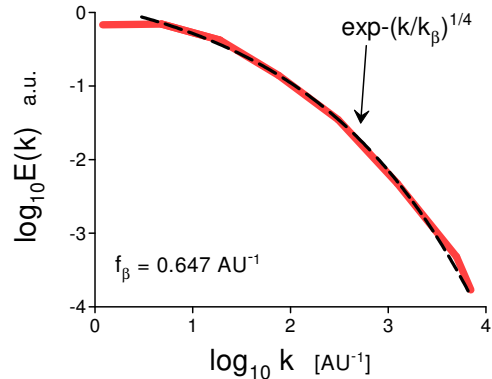


FIG. 7: The same as in Fig. 6 but at $1.5 < R < 2.8$ AU.

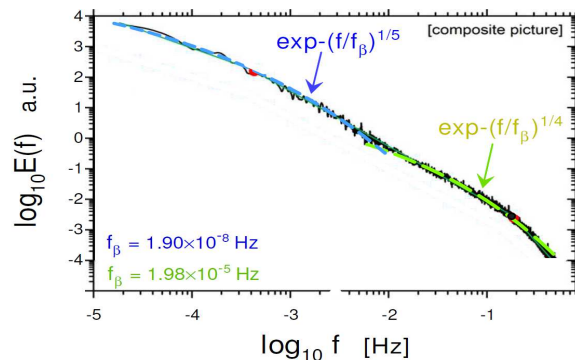


FIG. 8: Total magnetic energy spectrum for the fast solar wind at $R = 1.4$ AU (Ulysses).

for $2.8 < R < 4.5$ astronomical units (AU), where R is the distance from the Sun. The spectral data were rescaled by factor $4\pi R^2$ before averaging. Figure 7 shows analogous spectrum for $1.5 < R < 2.8$ AU (the spectral data were taken from the Fig. 3 of the Ref. [18]). The wavenumber spectra were obtained using Taylor's "frozen in" hypothesis. The dashed curves indicate correspondence to the stretched exponential spectrum Eq. (16).

Figure 8 shows the total magnetic energy spectrum for the fast solar wind at $R = 1.4$ AU computed using measurements made by the Ulysses mission. The spectral data were taken from Fig. 10 of the Ref. [20] (see Ref. [21]). The dashed curves indicate correspondence to the stretched exponential spectrum Eq. (17) for the large spatial scales (small frequencies in the figure) and to the stretched exponential spectrum Eq. (16) for the small spatial scales (large frequencies in the figure).

Space probe Helios 2 observed solar wind in the

ecliptic and much closer to the Sun [19]. Figure 9 shows the total magnetic energy spectrum for the fast solar wind at $R = 0.29\text{AU}$. The spectral data were taken from Fig. 24 of Ref. [20] (see Ref. [21]). The dashed curve indicates correspondence to the stretched exponential spectrum Eq. (17).

The NASA Parker Solar Probe studies the deeper inner heliosphere [22]. Figure 10 shows the magnetic energy spectrum computed from the auto-correlation of the magnetic field fluctuations measured at $R = 0.16\text{AU}$ (near Parker Solar Probe's first perihelion). The spectral data were taken from Fig. 1b of the Ref. [23]. Taylor's hypothesis was used to convert the time lags τ into the wavenumbers (in this figure $k = 1/V_0\tau$, where V_0 is the mean solar wind speed), and the wavenumber was taken in the units of the inverse ion inertial length $1/d_i$. The dashed curve indicates correspondence to the stretched exponential spectrum Eq. (17) for the large spatial scales. For the small spatial scales a Kolmogorov-like spectrum was observed (indicated by the straight line in the log-log scales).

V. TRANSITION FROM MAGNETOHYDRODYNAMICS TO KINETICS

A. Deterministic and distributed chaos in the transitional range of scales

As it was already mentioned the space can be considered as a plasmas laboratory with a broad spectrum of different situations. In paper Ref. [24], for instance, the transition from magnetohydrodynamics (large spatial scales) to kinetics (small spatial scales) in the solar wind was studied with emphasis on the effects related to the magnetic helicity.

Figure 11 shows the trace magnetic power spectrum measured at the Ulysses Northern Polar Pass ($R = 2.36\text{AU}$) in a fast (high-speed) solar wind. The spectral data were taken from Fig. 2 of the Ref. [24]. The dashed vertical line indicates the frequency position (using the Taylor's "frozen-in" hypothesis) of the thermal ion gyroradius ρ_i . The short-dash curve indicates correspondence to the exponential spectrum Eq. (5), i.e. to the deterministic chaos. The position of the characteristic frequency of the deterministic chaos f_c is indicated by the dotted arrow.

Figure 12 shows the power spectrum of magnetic fluctuations measured at $R = 1\text{AU}$ by ARTEMIS-P2 spacecraft. The spectral data were taken from Fig. 1 of Ref. [26]. The dashed curve indicates correspondence to the stretched exponential spectrum Eq. (17) - the distributed chaos. The ion gyroradius ρ_i and ion inertial length d_i are indicated in Fig. 12 by the vertical dotted lines. One can

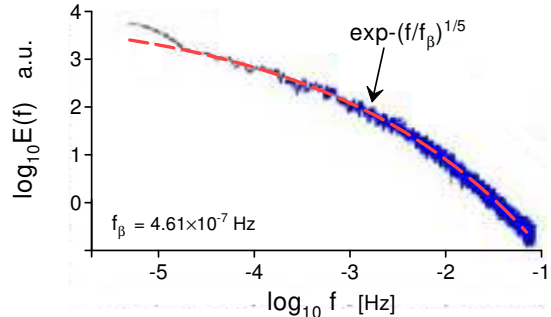


FIG. 9: Total magnetic energy spectrum for the fast solar wind at $R = 0.29\text{AU}$ (Helios 2, 1976y).

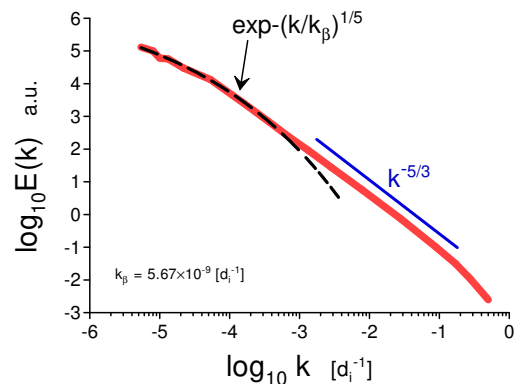


FIG. 10: Magnetic energy spectrum computed from the auto-correlation of the magnetic field fluctuations measured at $R = 0.16\text{AU}$ (near Parker Solar Probe first perihelion).

see that the magneto-inertial range covers scales transitional from magnetohydrodynamics to kinetics in this case.

B. Electron magnetohydrodynamics (EMHD)

There are different theoretical (numerical) models for this transitional range (see, for instance, Ref. [25] and references therein). If for the MHD scales one can treat the plasma as a single conducting fluid, for the transitional region a simple two-fluid model - electron magnetohydrodynamics (EMHD), can be applied as a first approximation. This model is rather appropriate for the cases dominated by the magnetic helicity [27]. It is assumed in the EMHD that ions provide only a motionless charge background for the fast electron flows which carry current and determine the dynamics of the magnetic field **B**

$$\mathbf{u}_e = -\frac{\mathbf{J}}{n_e e} = -\frac{c}{4\pi n_e e} [\nabla \times \mathbf{B}] \quad (22)$$

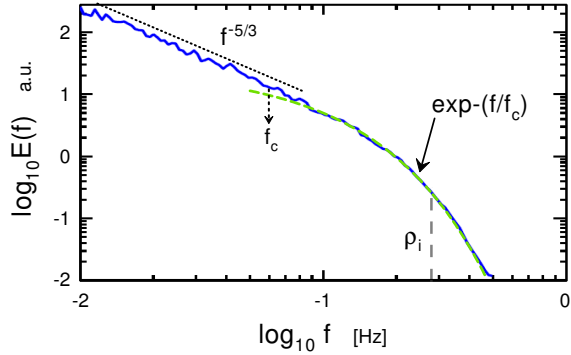


FIG. 11: Trace magnetic power spectrum measured at the Ulysses Northern Polar Pass ($R = 2.36$ AU).

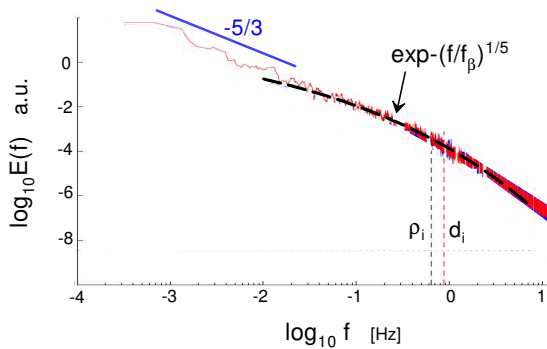


FIG. 12: Power spectrum of magnetic fluctuations measured at $R = 1$ AU.

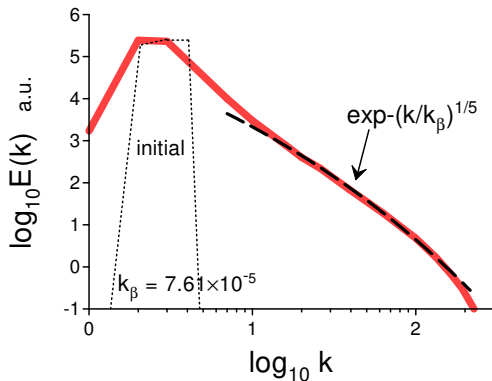


FIG. 13: Magnetic energy spectrum of the freely decaying positive EMHD wave packets at $t = 0.6$.

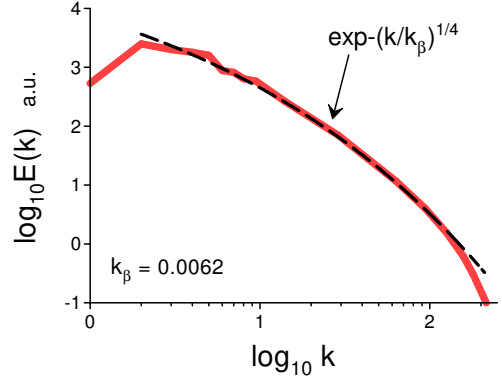


FIG. 14: As in the Fig. 13 but for negative EMHD wave packets.

where \mathbf{J} is the electric current density, \mathbf{u}_e is the electron velocity, n_e is the electron number density [28].

Substitution of the Eq. (22) into the equation

$$\frac{\partial \mathbf{B}}{\partial t} = \nabla \times [\mathbf{u}_e \times \mathbf{B}] + \eta \nabla^2 \mathbf{B} \quad (23)$$

provides an equation describing the dynamics of the magnetic field in the incompressible EMHD

$$\frac{\partial \mathbf{B}}{\partial t} = -\frac{c}{4\pi n_e e} \nabla \times [(\nabla \times \mathbf{B}) \times \mathbf{B}] + \eta \nabla^2 \mathbf{B} \quad (24)$$

It should be noted that magnetic helicity for the EMHD is conserved in the ideal case similar to the MHD [25]. Unlike the MHD Alfvén waves the EMHD waves are helical and carry a nonzero magnetic helicity. Also, the EMHD waves are dispersive and can interact with each other. In a strong imposed magnetic field the direction of propagation of the EMHD wave packets is either parallel or antiparallel to the magnetic field lines. One can speak about ‘positive’ and ‘negative’ wave packets in respect to the sign of the magnetic helicity carried by the wave packets.

In the Ref. [27] the Eq. (24) was solved numerically in a periodic box for the decaying case with an imposed uniform magnetic field \mathbf{B}_0 (so that $\mathbf{B} = \mathbf{B}_0 + \mathbf{b}$). Figure 13 shows the power spectrum of magnetic energy of the freely decaying positive EMHD wave packets obtained with this DNS (the spectral data were taken from Fig. 4 of the Ref. [27] for $t = 0.6$ in the terms of the Ref. [27]). The dotted lines show the initial energy spectrum (only positive waves were present in the DNS at $t = 0$). The dashed curve indicates the stretched exponential spectrum Eq. (17).

The EMHD wave packets moving in one direction interact with each other and, therefore, can generate counterpropagating waves. Figure 14 shows the power spectrum of magnetic energy of the freely decaying

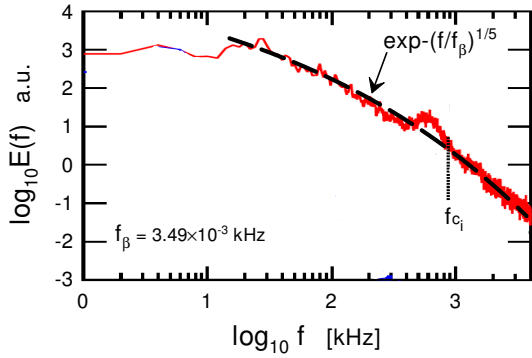


FIG. 15: Power spectrum of the vertical component of the magnetic field measured within the plasma edge.

negative EMHD wave packets obtained with this DNS (the spectral data were taken from Fig. 4 of the Ref. [27] for $t = 0.6$). The dashed curve indicates the stretched exponential spectrum Eq. (16).

C. Reconnections in the laboratory and in Earth's magnetosphere

In recent Ref. [29] results of an experiment with local magnetic helicity injection into a toroidal system (a spherical tokamak startup) have been reported and the physical mechanisms converting the injected magnetic helicity into a large-scale current drive are experimentally studied. In this experiment, the intense electron current sources inject the magnetic helicity at the edge of a tokamak. Magnetic reconnections associated with the helicity-conserving instabilities convert the topology of the open field lines into a tokamak-like toroidal one.

Figure 15 shows the power spectrum of the vertical component of the magnetic field measured within the plasma edge. The spectral data were taken from Fig. 1 of the Ref. [29]. The position of the local ion cyclotron frequency f_{c_i} is indicated by the dotted vertical line. The dashed curve indicates the stretched exponential spectrum Eq. (17).

In paper Ref. [30] results of measurements with four Cluster spacecraft in the plasma sheet of the Earth's magnetosphere were reported. The event under consideration was a high-speed reconnection jet with a moderate mean (guide) magnetic field. Figure 16 shows the power spectrum of the magnetic field measured during the reconnection event. The position of the proton cyclotron frequency f_{c_p} is indicated by the vertical dotted arrow. The dashed curve indicates the stretched exponential spectrum Eq. (17).

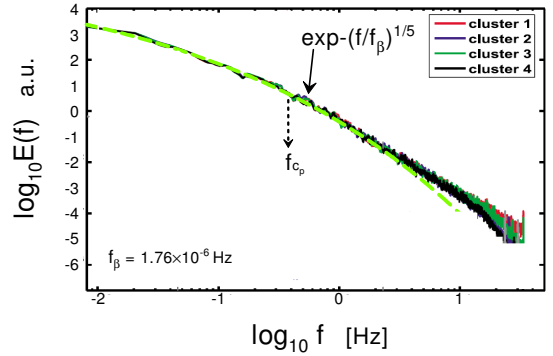


FIG. 16: Power spectrum of the magnetic field measured in the magnetospheric reconnection jet.

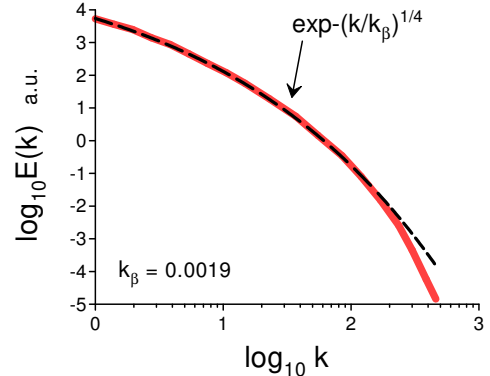


FIG. 17: Magnetic energy spectra for the freely decaying MHD turbulence with considerable mean magnetic helicity (DNS).

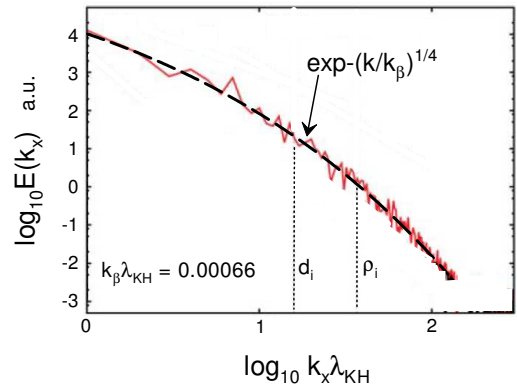


FIG. 18: Power spectrum of a magnetic field component computed in the numerical simulation and corresponding to the magnetic field component normal to the nominal magnetopause in the MMS observations.

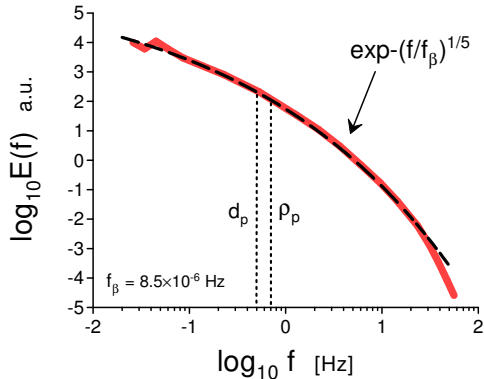


FIG. 19: Power spectrum of the magnetic field component normal to the nominal magnetopause measured by the MMS for the Kelvin-Helmholtz active period.

D. Kelvin-Helmholtz vortices at the Earth's magnetopause

The Kelvin-Helmholtz vortices (or the flow shear-driven Kelvin-Helmholtz instability) at Earth's magnetopause can be a significant factor for the transport of momentum and mass from the solar wind environment into Earth's magnetosphere (see, for instance, Ref. [31] and references therein).

Let us begin with the Kelvin-Helmholtz instability in turbulent MHD flows. In the paper Ref. [32] results of direct numerical simulation of a freely decaying 3D MHD flow (Eqs. (18-21) with $\mathbf{f} = 0$) with a superposition

of random and deterministic (three ABC flows) initial conditions and considerable mean magnetic helicity were reported. The Kelvin-Helmholtz instabilities with rolling up of current and vorticity sheets were observed at a high Reynolds number ($Re = 10100$). Figure 17 shows magnetic energy spectra for $t = 1.6$ in the terms of the Ref. [32] (the spectral data were taken from Fig. 2b of the Ref. [32]). The dashed curve indicates the stretched exponential spectrum Eq. (16).

In recent Ref. [33] results of a 3D kinetic simulation of the Kelvin-Helmholtz instability, with the conditions relevant to the Magnetospheric Multiscale spacecraft (MMS) observations in the Earth's magnetopause [31], were reported. Figure 18 shows the power spectrum of a magnetic field component computed in the numerical simulation and corresponding to the magnetic field component normal to the nominal magnetopause in the MMS observations. The spectral data were taken from Fig. 4b of the Ref. [31]. The ion gyroradius ρ_i and ion inertial length d_i are indicated in Fig. 18 by the vertical dotted lines. The dashed curve indicates the stretched exponential spectrum Eq. (16).

In the Ref. [31] results of measurements produced by the Magnetospheric Multiscale spacecraft (MMS) in the Kelvin-Helmholtz vortices at the magnetopause (the outer boundary of Earth's magnetosphere) were reported. Figure 19 shows the corresponding power spectrum of the magnetic field component perpendicular to the mean magnetic field and normal to the nominal magnetopause for the Kelvin-Helmholtz active period. The spectral data were taken from Fig. 3a of the Ref. [31]. The proton gyroradius ρ_p and proton inertial length d_p are indicated in Fig. 19 by the vertical dotted lines. The dashed curve indicates the stretched exponential spectrum Eq. (17).

-
- [1] W.H. Matthaeus and M.L. Goldstein, *J. Geophys. Res.*, **87**, 6011 (1982).
 - [2] A.S. Monin, A.M. Yaglom, *Statistical Fluid Mechanics, Vol. II: Mechanics of Turbulence* (Dover Pub. NY, 2007).
 - [3] U. Frisch and R. Morf, *Phys. Rev.*, **23**, 2673 (1981).
 - [4] A. Brandstater and H. L. Swinney, *Phys. Rev. A* **35**, 2207 (1987).
 - [5] J. E. Maggs and G. J. Morales, *Phys. Rev. Lett.* **107**, 185003 (2011); *Phys. Rev. E* **86**, 015401(R) (2012); *Plasma Phys. Control. Fusion* **54** 124041 (2012).
 - [6] S. Khurshid, D.A. Donzis, and K.R. Sreenivasan, *Phys. Rev. Fluids*, **3**, 082601(R) (2018).
 - [7] W. Gekelman et al., *Plasma Phys. Control. Fusion*, **56**, 064002 (2014).
 - [8] D.A. Schaffner, M.R. Brown, and V.S. Lukin, *ApJ*, **790**, 126 (2014).
 - [9] M.A. Berger and G.N. Field, *J. Fluid Mech.*, **147**, 133 (1984).
 - [10] T.H. Jensen and M.S. Chu, *Phys. Fluids*, **27**, 2881 (1984).
 - [11] T. DeHaas, and W. Gekelman, *Phys. Plasmas*, **24**, 072108 (2017).
 - [12] T. Amari, J.F. Luciani, J.J. Aly, Z. Mikic, and J. Linker, *ApJ*, **595**, 1231 (2003).
 - [13] V. Abramenko, V. Yurchyshyn, H. Wang, P.R. Goode, *Solar Physics*, **201**, 225 (2001).
 - [14] A. Bershadskii, *Res. Notes AAS*, **4**, 10 (2020).
 - [15] R.S. Iroshnikov, *Astronomicheskii Zhurnal*, **40**, 742 (1963) (English translation in *Soviet Astronomy* **7**, 566 (1964)).
 - [16] D.C. Johnston, *Phys. Rev. B*, **74**, 184430 (2006).
 - [17] K. Yoshimatsu, K. Schneider, N. Okamoto, Y. Kawahara, and M. Farge, *Phys. Plasmas*, **18**, 092304 (2011).
 - [18] A. Brandenburg, K. Subramanian, A. Balogh, M.L. Goldstein, *ApJ*, **734**, 9 (2011).
 - [19] H. Rosenbauer, R. Schwenn, E. Marsch, E., et al., *J.*

- Geophysics Zeitschrift Geophysik, **42**, 561 (1977)
- [20] R. Bruno, Parker Solar Probe SWG Meeting Join with Solar Orbiter, JHU-APL, Laurel, MD, USA (2017).
- [21] <https://slideplayer.com/slide/13620181/>
- [22] N.J Fox, M.C. Velli, S.D. Bale, R. Decker, A. Driesman, R.A. Howard, J.C. Kasper, J. Kinnison, M. Kusterer, D. Lario, D.; et al., Space Sci. Rev., **204**, 7 (2016).
- [23] M.E. Cuesta, T.N. Parashar, R. Chhiber, and W.H. Matthaeus, arXiv:2202.01874 (2022).
- [24] J.J. Podesta and S.P. Gary, ApJ, **734**, 15 (2011).
- [25] A.A. Schekochihin, S.C. Cowley, W. Dorland, G.W.Hammett, G.G.Howes, E. Quataert and T. Tatsuno, Astrophys. J. Suppl. Ser., **182**, 310 (2009).
- [26] C.H.K. Chen, S. Boldyrev, Q. Xia, and J.C. Perez, Phys. Rev. Lett., **110**, 225002 (2013).
- [27] J. Cho and H. Kim, J. Geophys. Res. Space Physics,, **121**, 6157 (2016).
- [28] A.S. Kingsep, K V. Chukbar, and V.V. Yankov, Rev. Plasma Phys., **16**, (1990).
- [29] N.J. Richner, G.M. Bodner, M.W. Bongard , R.J. Fonck , M.D. Nornberg , and J.A. Reusch, Phys. Rev. Lett., **128**, 105001 (2022).
- [30] S.Y. Huang, M. Zhou, and F. Sahraoui et al., Geophys. Res. Lett., **39**, L11104 (2012).
- [31] H. Hasegawa, T.K.M. Nakamura, D.J. Gershman, Y. Nariyuki, A.F. Vinas, et al., JGR: Space Physics, **125**, e2019JA027595 (2020).
- [32] P.D. Mininni, A.G. Pouquet, and D.C. Montgomery, Phys. Rev. Lett., **97**, 244503 (2006).
- [33] T.K.M. Nakamura, The Earth's low-latitude boundary layer, in Magnetospheres in the Solar System (eds. R. Maggiolo, N. Andre, H. Hasegawa, and D. Welling), John Wiley & Sons, Inc, Hoboken, NJ (2020).